NUMERICAL GENERATION AND ABSORPTION OF FULLY NONLINEAR PERIODIC WAVES

By Stéphan T. Grilli,[1] Member, ASCE, and Juan Horrillo[2]

ABSTRACT: Permanent form periodic waves with zero-average mass flux are generated in a two-dimensional numerical wave tank solving fully nonlinear potential flow equations. An absorbing beach is modeled at the end of the tank in which (1) an external free-surface pressure absorbs energy from high frequency waves; and (2) a pistonlike condition absorbs energy from low-frequency waves. A feedback mechanism adaptively calibrates the beach parameters to absorb the period-averaged energy of incident waves. Wave generation and absorption are validated over constant depth, for tanks and beaches of various lengths, and optimal parameter values are identified for which reflection from the beach is reduced to a few percent. Shoaling of periodic waves is then modeled over a 1:50 slope, up to very close to the breaking point. A quasi-steady state is reached in the tank for which (not previously calculated) characteristics of fully nonlinear shoaling waves are obtained.

INTRODUCTION

Nonlinear Wave Modeling

Over the past 20 years, considerable efforts were devoted to developing increasingly accurate and efficient models for fully nonlinear surface waves. Most successful models so far were based on potential flow theory with fully nonlinear free-surface boundary conditions [i.e., a fully nonlinear potential flow (FNPF)]. Such models were successfully applied to periodic wave propagation and overturning in deep water and to solitary wave shoaling, up to breaking over slopes, with a surprising degree of accuracy (Dommermuth et al. 1988; Grilli et al. 1994).

In most FNPF models to date, the governing (Laplace's) equation has been solved with a higher-order boundary element method (BEM) (Brebbia 1978), either based on Green's identity or on Cauchy integral theorem formulations, and on time-integrating the free-surface boundary conditions (expressed in a mixed Eulerian-Lagrangian formulation) either using a time-marching predictor-corrector (Longuett-Higgins and Cokelet 1976, LC) or a Taylor series expansion, method (Dold and Peregrine 1986, DP). Early computations following this approach were restricted to space-periodic waves over constant depth (LH; DP; New et al. 1985; Vinje and Brevig 1981) but more recent models can accommodate both arbitrary incident waves and complex bottom topography [e.g., Klopman (1988); Grilli et al. (1989) (GSS); Cointe (1990); Cooker (1990); Ohyama and Nadaoka (1991)]. Most recent models also directly work in a physical space region, that is, a numerical wave tank (NWT), in which incident waves are generated at one extremity and reflected, absorbed, or radiated at the other extremity.

GSS's FNPF model is used in the present study. Many validations (both analytical and experimental) of this model and of its later improved versions were carried out, mostly for solitary waves [e.g., Grilli and Svendsen (1990) (GS); Svendsen and Grilli (1990); Grilli et al. (1994, 1997)].

Wave Generation

Numerical wavemakers (WMs) were used by many authors to generate waves in FNPF models (e.g., Lin et al. (1984); Dommermuth et al. (1988); GSS; Cointe (1990)]. [Note, Brorsen and Larsen (1987) proposed a different approach, using internal sources for generating waves, which was also used by Ohyama and Nadaoka (1994).] In this case, there is a corner at the intersection between the WM and the free surface, where a singularity of the solution may occur during a so-called cold start. To eliminate such singularities, GS, Otta et al. (1992), and Grilli and Subramanya (1996) (GSU) introduced (1) an initial tapering of the WM motion, ensuring that the acceleration remains small during the first few time steps of the computations; (2) a double-node representation of the corner, with continuity and compatibility relationships for the potential and the velocity at both nodes; and (3) an exponentially decaying initial free-surface elevation satisfying linearized boundary conditions at the first time step. These methods are used in the present calculations.

Assuming no singularity occurs at the corner, it is well known that steadily progressing finite-amplitude waves cannot be generated in finite depth with a WM, whether in laboratory tanks or in nonlinear wave models [see, e.g., Mei (1989, p. 578); Chapalain et al. (1992)]: resonant nonlinear interactions will occur and create higher-order harmonics modulating the shape of the wave. [This mechanism occurs right at the start of wave generation and is different from the so-called sideband instability affecting large finite-amplitude waves after long distances of propagation, see, for example, Mei (1989, p. 620). Also note that second-order corrections to the WM motion have been proposed, e.g., by Schäffer (1996).] To overcome this difficulty, Klopman (1988) generated exact periodic waves in his model, that is, stream-function waves (SFWs) [e.g., Dean and Dalrymple (1984, p. 305)], by specifying their horizontal velocity along a vertical wavemaking boundary (WB). Unlike linear waves, SFWs have a nonzero horizontal mass flux and, hence, there is a net mean flow through the WB that gradually increases the volume of the computational domain. In Klopman's study, this did not pose a problem since his wave-breaking computations only lasted a short time. In shoaling computations over gentle slopes, for a larger number of wave periods, however, this will result in a significant increase in the mean water level, which affects wave shape in a nonphysical manner. For the corresponding coastal problem, one would indeed expect an undertow current to occur and cancel the incoming wave mass flux at some distance from the shore, thereby ensuring constant water volume in the nearshore region. Hence, in the present paper, a method is proposed for achieving zero-average-mass flux in the generation of SFWs.

Wave Absorption

Various radiation or absorption boundary conditions (RABCs) were proposed to dissipate incident wave energy in

[1]Assoc. Prof., Oc. Engrg. Dept., Univ. of Rhode Island, Narragansett, RI 02882.

[2]Grad. Res. Asst., Oc. Engrg. Dept., Univ. of Rhode Island, Narragansett, RI.

Note. Associate Editor: James T. Kirby. Discussion open until March 1, 1998. To extend the closing date one month, a written request must be filed with the ASCE Manager of Journals. The manuscript for this paper was submitted for review and possible publication on July 28, 1995. This paper is part of the *Journal of Engineering Mechanics*, Vol. 123, No. 10, October, 1997. ©ASCE, ISSN 0733-9399/97/0010-1060–1069/ $4.00 + $.50 per page. Paper No. 11261.

NWTs. These were mostly based on the RABCs by Sommerfeld (1949), Le Mehauté (1972), Orlanski (1976), Engquist and Majda (1977), and Israeli and Orszag (1981) [see review by Romate (1992)]. Although some of these conditions are exact for linear waves or weakly nonlinear long waves, no general method has yet been proposed for the radiation of fully nonlinear transient waves. Rather heuristic boundary conditions have been used instead [see, e.g., Clément (1996) for further discussions]. Lin et al. (1984), for instance, matched exterior linear solutions to the nonlinear interior solution at finite distance. GSS developed an implicit iterative radiation condition, based on Sommerfeld's condition. Otta et al. (1992) proposed a more accurate explicit approach based on a Sommerfeld/Orlanski condition. Based on Le Mehauté's work, Larsen and Dancy (1983) introduced the idea of an "absorbing beach" (AB), in which an external counteracting pressure is specified over the free surface to create a negative work against incident waves. They only implemented the method in a (weakly nonlinear) Boussinesq model, but the same method was later used in FNPF models by Cointe (1990), Cao et al. (1993), Ohyama and Nadaoka (1994), Subramanya and Grilli (1994), and Clément (1996).

Observing that radiation type methods perform well for low-frequency waves, whereas ABs do so for high-frequency waves, some authors successfully combined both approaches [e.g., Ohyama and Nadaoka (1991, 1994)]. Along this line, Clément (1996) proposed to combine an AB with a new, pistonlike, absorbing boundary condition at the tank extremity, and showed that the method performed well for unsteady finite-amplitude waves. In the present paper, an improved formulation of Clément's method is proposed, in which the AB coefficient is adaptively calibrated in time to absorb the period-averaged energy of incident waves entering the beach.

MATHEMATICAL AND NUMERICAL MODELS

Governing Equations and Numerical Algorithms for FNPF Model

Equations for GSS/GS's two-dimensional FNPF wave model are briefly presented in the following. The velocity potential $\phi(\mathbf{x}, t)$ is used to describe inviscid irrotational flows in the vertical plane (x, z) and the velocity is defined by, $\mathbf{u} = \nabla\phi = (u, w)$. The continuity equation in the fluid domain $\Omega(t)$ with boundary $\Gamma(t)$ is a Laplace's equation for the potential (Fig. 1)

$$\nabla^2\phi = 0 \quad \text{in} \quad \Omega(t) \tag{1}$$

On the free surface $\Gamma_f(t)$, ϕ satisfies the kinematic and dynamic boundary conditions

$$\frac{D\mathbf{r}}{Dt} = \left(\frac{\partial}{\partial t} + \mathbf{u}\cdot\nabla\right)\mathbf{r} = \mathbf{u} = \nabla\phi \quad \text{on} \quad \Gamma_f(t) \tag{2}$$

$$\frac{D\phi}{Dt} = -gz + \frac{1}{2}\nabla\phi\cdot\nabla\phi - \frac{p_a}{\rho} \quad \text{on} \quad \Gamma_f(t) \tag{3}$$

respectively, where $\mathbf{r}$ = position vector on the free surface; g = gravitational acceleration; z = vertical coordinate; p_a = pressure at the free surface; and ρ = fluid density. Along the stationary bottom Γ_b, the no-flow condition is prescribed as

$$\frac{\overline{\partial\phi}}{\partial n} = 0 \quad \text{on} \quad \Gamma_b \tag{4}$$

where the overbar denotes specified values. Boundary conditions for wave generation and absorption are presented in the next sections.

Eq. (1) is transformed into a boundary integral equation (BIE), using Green's second identity, and solved by a BEM. The BIE is thus evaluated at N discretization nodes on the boundary, and M higher-order elements are defined to interpolate in between discretization nodes. In the present applications, quadratic isoparametric elements are used on lateral and bottom boundaries, and cubic elements ensuring continuity of the boundary slope are used on the free surface. In these elements, referred to as mixed cubic interpolation (MCI) elements, geometry is modeled by cubic splines, and field variables are interpolated between each pair of nodes, using the midsection of a four-node "sliding" isoparametric element. Expressions of BEM integrals (regular, singular, quasi-singular) are given in GSS, GS, and Grilli and Subramanya (1994, 1996), for isoparametric and MCI elements.

Free-surface boundary conditions (2) and (3) are time-integrated based on two second-order Taylor series expansions expressed in terms of a time step Δt and of the Lagrangian time derivative, D/Dt, for ϕ and $\mathbf{r}$. First-order coefficients in the series correspond to free-surface conditions (2) and (3), in which ϕ and $\partial\phi/\partial n$ are obtained from the solution of the BIE for $(\phi, \partial\phi/\partial n)$ at time t. Second-order coefficients are expressed as D/Dt of (2) and (3), and are calculated using the solution of a second BIE for $(\partial\phi/\partial t, \partial^2\phi/\partial t\partial n)$, for which boundary conditions are obtained from the solution of the first problem. Detailed expressions for the Taylor series are given in GSS.

At each time step, global accuracy of computations is verified by computing errors in total volume and energy for the generated wave train. GS showed that these errors are a function of both the size (i.e., distance between nodes) and the degree (i.e., quadratic, cubic, . . .) of boundary elements used in the spatial discretization, and of the size of the selected time step. They thus proposed a method for adaptively selecting the optimal time step, based on a mesh Courant number $C_o(t)$. For

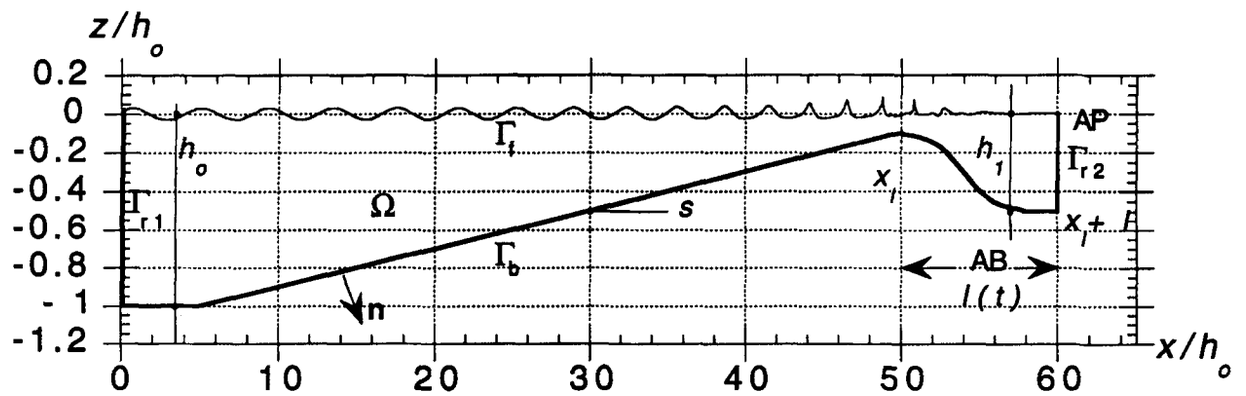

FIG. 1. Computational Domain for Periodic Wave Shoaling over Gentle Slope s [an AB of Length $l(t)$ and Maximum Depth h_1, Is Specified on Free Surface $\Gamma_f(t)$ for $x > x_l$; an AP Is Specified at $x_p(t) = x_l + l(t)$]

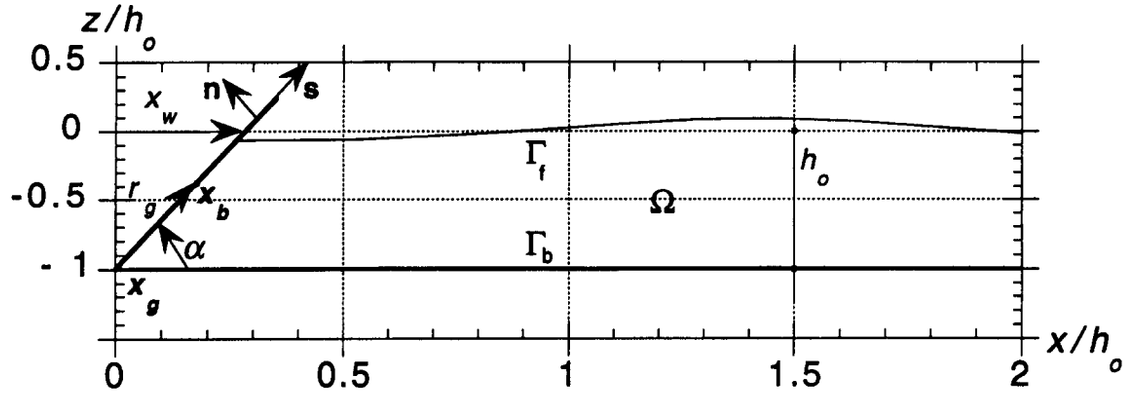

FIG. 2. Sketch and Definitions for Flap WM Motion Specified on Boundary Γ_{r1} of Computational Domain

the MCI elements, GSU showed that the optimum value of C_o is around 0.40. This value is used in the present applications.

Periodic Wave Generation in Model

Flap Wavemaker

For a flap WM on boundary $\Gamma_{r1}(t)$, continuity of normal velocity yields the following boundary conditions (Fig. 2):

$$\overline{\frac{\partial \Phi}{\partial n}} = r_g \dot{\alpha}; \quad \overline{\frac{\partial^2 \Phi}{\partial t \partial n}} = r_g \ddot{\alpha} + \dot{\alpha}\left[r_g \frac{\partial^2 \Phi}{\partial s^2} - \frac{\partial \Phi}{\partial s}\right] \quad \text{on} \quad \Gamma_{r1}(t) \tag{5a,b}$$

where r_g and $\alpha(t)$ = distance to the center of rotation, $\mathbf{x}_g = (0, -h_o)$, and the angle of rotation of the WM, respectively. Time derivatives of α (upper dots) can be expressed as a function of WM stroke $x_w(t)$ and of its time derivatives.

Using (5), a periodic wave of frequency ω can, for instance, be generated in the model (keeping in mind that higher-order harmonics will also occur) by specifying the stroke as, $x_w(t) = S[1 - \cos \omega t]/2$, in which the maximum stroke S can be estimated as a function of wave height H and frequency based on a WM theory [e.g., Dean and Dalrymple (1984)]. To avoid initial singularity problems, $x_w(t)$ is multiplied by a tapering function varying from 0 to 1 over a specified time.

Exact Wave Generation

SFW theory calculates "numerically exact" periodic solutions of the FNPF problem in depth h_o. In a coordinate system moving with the wave celerity $c = L/T$, the stream function is modeled as

$$\psi(\theta, z) = \sum_{j=1}^{n} X(j) \sinh jk(h_o + z) \cos j\theta - (U - c)z \tag{6}$$

where $\theta = k(x - ct)$ is the phase; U = a uniform current; and $X(j)$ = a set of n numerical coefficients calculated, together with wavelength $L = 2\pi/k$, to satisfy free-surface boundary conditions (2) and (3), and specified wave height and period (H, T). Horizontal velocity is obtained from (6) in the original coordinate system as

$$u(\theta, z) = -\frac{\partial \psi}{\partial z} + c = -\sum_{j=1}^{n} (jk) X(j) \cosh jk(h_o + z) \cos j\theta + U \tag{7}$$

and, noting that $\partial\theta/\partial t = -ck$, local horizontal acceleration is obtained as

$$\frac{\partial u}{\partial t} = -c \sum_{j=1}^{n} (jk)^2 X(j) \cosh jk(h_o + z) \sin j\theta \tag{8}$$

Eqs. (7) and (8) are used to specify the kinematics of an incident SFW over a vertical wavemaking boundary (WB), $\Gamma_{r1}(t)$, at $x = x_w$ (Fig. 1).

Free-surface discretization nodes represent fluid particles which, for nonlinear waves, gradually drift away in the direction of the mean mass transport, eventually leading to a poor resolution close to the WB. This drift is cancelled by horizontally moving the WB with the Lagrangian motion, $x_w(t) = x_1(t)$, of the first node/particle on the free surface.

As for the flap wavemaker, the initial velocity field is multiplied by a ("tanh-like") tapering function $D(t)$, smoothly varying from 0 to 1 over a specified number of wave periods. Boundary conditions on the WB thus read

$$\overline{\frac{\partial \Phi}{\partial n}} = -u(\theta, z) D(t) \text{ on } \Gamma_{r1}(t) \equiv (x = x_w(t);\ z \in \{-h_o, \eta[x_w(t)]\}) \tag{9a}$$

$$\overline{\frac{\partial^2 \Phi}{\partial t \partial n}} = -u(\theta, z)\dot{D}(t) - \frac{\partial u}{\partial t}(\theta, z) D(t) \tag{9b}$$

where $\theta(t) = k[x_w(t) - ct] - \theta_o$ (with θ_o a phase shift to the point of zero up-crossing); $x_w(t) = x_1(t)$, $\eta[x_w(t)] = z_1(t)$; and u and $\partial u/\partial t$ are calculated with (7) and (8), using both the coefficients $X(j)$ and the wave characteristics obtained from the SFW solution, (6).

Zero-Mass Flux Condition for Exact Waves

The mean wave mass transport M_o and mass transport velocity $\overline{U_o}$ are defined as (Dalrymple 1976)

$$M_o = \rho \frac{1}{T} \int_0^T \left[\int_{-h_o}^{\eta} u(x_o, z, t)\, dz \right] dt \quad \text{and} \quad \overline{U_o} = \frac{M_o}{\rho h_o} \tag{10}$$

where $\eta(x_o, t)$ denotes the instantaneous free-surface elevation at an arbitrary location x_o.

To eliminate unwanted volume increase in the computational domain due to mean flow through the WB, incident SFWs are simultaneously generated with a uniform current U, equal and opposite to $\overline{U_o}$. Such waves are referred to as zero-mass-flux SFWs. Since a current slightly modifies wave characteristics due to Doppler effect, U must be iteratively calculated, for specified wave height H_o and period T, together with wavelength L and streamfunction coefficients $X(j)$, to satisfy a zero-mass-flux condition. Moreover, in this calculation, one must also account for the motion of the WB, following the first free-surface particle $x_o = x_w(t)$. This implies that the Lagrangian wave period T_L must be used for the time integral in (10), and, hence, the zero-mass-flux condition in the SFW generation reads

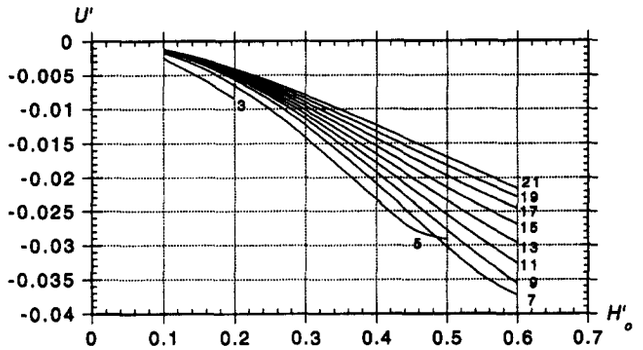

FIG. 3. Opposite Mean Current U', for Zero-Mass-Flux SFW Generation in Depth h_o; Numbers on Curves Denote Wave Period T'

$$h_o \Delta x_w - \int_0^{T_L} [h_o + \eta_w(t)] u_w(t)\, dt + \int_0^{T_L} \left\{ \int_{-h_o}^{\eta_w(t)} u[x_w(t), z, t]\, dz \right\} dt = 0 \tag{11}$$

where $\eta_w(t) = \eta[x_w(t)]$ and $u_w(t) = u[x_w(t), \eta_w(t)]$ are the elevation and the horizontal velocity of the first free surface node/particle, respectively, and

$$T_L = T\left(1 + \frac{\Delta x_w}{L}\right) \quad \text{with} \quad \Delta x_w = \int_0^{T_L} u_w(t)\, dt \tag{12}$$

where Δx_w = horizontal displacement of the WB over time T_L (same as first free-surface particle). Eq. (11) expresses a volume balance over time T_L: the first term is the volume change due to net WB motion; the second term is the volume change due to horizontal velocity of the first free surface particle; and the third term is the total wave Lagrangian mass transport. Eqs. (11) and (12) are iteratively used to calculate U and $[L, X(j)]$ for a SFW of given characteristics. Incident waves are then generated by specifying the SFW's kinematics in (9). Fig. 3 shows U as a function of dimensionless wave characteristics (H_o', T'). [In dimensionless (prime) variables, lengths are divided by h_o and times by $\sqrt{h_o/g}$.] As expected, results show increasing effects of nonlinearity on U' (i.e., $|U'|$ increases for increasing H_o' and decreasing T').

Finally, since the horizontal particle velocity is larger at the free surface than on the bottom, despite the correction by the depth-averaged mean current U, the WB still has a small average net forward motion as a function of time. This is illustrated in the applications.

Wave Energy Absorption in Model

Absorbing Beach

An external counteracting pressure $p_a = P$ is specified in the dynamic free surface condition (3) (with $z = \eta$) to create a negative work, and thus absorb wave energy over a given section Γ_l of the free surface. To create additional wave reduction through deshoaling in the AB, the bottom geometry is specified somewhat similar to a natural bar (Fig. 1).

In most ABs proposed earlier, P was specified as proportional to the free-surface potential ϕ. Cao et al. (1993), however, showed that this could create a positive work in some cases and suggested instead to define the external pressure as proportional to the normal particle velocity. This method is used in the present computations. The modified dynamic free-surface condition in the AB thus reads

$$\frac{D\phi}{Dt} - \frac{1}{2}\nabla\phi\cdot\nabla\phi + g\eta + \frac{P}{\rho} = 0 \quad \text{on} \quad \Gamma_l(t) \tag{13}$$

with

$$P(x, \eta, t) = \nu(x, t)\frac{\partial\phi}{\partial n}[\eta(x, t)] \tag{14}$$

where ν, the beach absorption function, is smoothly varied along the AB as

$$\nu(x, t) = \nu_o(t)\rho\sqrt{gh_1}\left(\frac{x - x_l}{l}\right)^{\mu} \tag{15}$$

where μ = 2 to 3; ν_o = a nondimensional beach absorption coefficient; and h_1 = maximum depth in the AB.

Absorbing Piston

Clément (1996) showed that ABs only absorb high-frequency waves well. To absorb low-frequency waves, he proposed use of a pistonlike boundary condition at the tank extremity, $x_p = x_l + l(t)$ [absorbing piston (AP); Fig. 1]. Developing Clément's AP condition for boundary $\Gamma_{r2}(t)$, we obtain, for the piston velocity

$$u_p[x_p(t)] = \frac{1}{\rho h_1\sqrt{gh_1}}\int_{-h_1}^{\eta_p(t)} p_D[x_p(t), z]\, dz \tag{16}$$

where p_D = dynamic pressure; and the integral represents the horizontal hydrodynamic force F_{D_p} acting on the piston at time t. To avoid drift of the piston with time, the dynamic pressure is linearized to $p_D = -\rho\partial\phi/\partial t$. In the numerical model, the AP boundary condition (16) is implemented as follows:

$$u_p(t + \Delta t) = \left[\frac{1}{\rho h_1\sqrt{gh_1}}F_{D_p}(t) + u_p(t)\right]\Big/2 \tag{17a}$$

$$x_p(t + \Delta t) = x_p(t) + u_p(t)\Delta t + \frac{Du_p}{Dt}(t)\frac{(\Delta t)^2}{2} \tag{17b}$$

$$\overline{\frac{\partial\phi}{\partial n}}[x_p(t + \Delta t)] = u_p(t + \Delta t) \tag{17c}$$

$$\overline{\frac{\partial^2\phi}{\partial t\partial n}}[x_p(t + \Delta t)] = \frac{Du_p}{Dt}(t + \Delta t) - u_p(t + \Delta t)\frac{\partial^2\phi}{\partial s^2}(t + \Delta t) \quad \text{on} \quad \Gamma_{r2}(t) \tag{17d}$$

where the moving average in the first equation is introduced to avoid numerical oscillations, and Du_p/Dt is calculated as a second-order finite difference approximation.

Adaptive Calibration of Absorption Coefficient

The AB coefficient ν_o is usually specified as a constant [e.g., Cointe (1990)]. Wave energy absorption, however, can be optimized by adaptively calculating ν_o for the AB to absorb the period-averaged energy entering the beach at $x = x_l$ over time step Δt, that is, $\overline{E_f}(t)\Delta t$, minus that leaving the beach at the AP, with $\overline{E_f}$ the period-averaged wave energy flux calculated as

$$\overline{E_f}(t) = -\frac{\rho}{T}\int_{t-T}^{t}\left[\int_{-h(x_l)}^{\eta(x_l,\tau)}\frac{\partial\phi}{\partial t}(x_l, z, \tau)\frac{\partial\phi}{\partial x}(x_l, z, \tau)\, dz\right] d\tau \tag{18}$$

Energy absorption along the AB free surface and along the AP corresponds to the work of the external and hydrodynamic pressures, respectively. Over Δt, in average, this work is equal to $\overline{E_{fa}}(t)\Delta t$, with

$$\overline{E_{fa}}(t) = \frac{1}{T}\int_{t-T}^{t}\left\{\int_{\Gamma_f(\tau)} P[\eta(x,\tau)]\,\frac{\partial\phi}{\partial n}\,[\eta(x,\tau)]\,d\Gamma + F_{D_p}(\tau)u_p(\tau)\right\}d\tau \tag{19}$$

the instantaneous period-averaged energy flux absorbed in the AB/AP. The instantaneous value of the beach coefficient ν_o can thus be found by simply balancing energy input and energy absorption: $\overline{E_f} = \overline{E_{fa}}$, which by (14)–(19) leads to

$$\nu_o(t) = \frac{\overline{E_f}(t) - \frac{1}{T}\int_{t-T}^{t} F_{D_p}(\tau)u_p(\tau)\,d\tau}{\left[\rho\sqrt{gh_1}\,\frac{1}{T}\int_{t-T}^{t}\left(\int_{\Gamma_f(\tau)}\left\{\frac{\partial\phi}{\partial n}\,[\eta(x,\tau)]\right\}^2\left(\frac{x-x_l}{l}\right)^{\mu}d\Gamma\right)d\tau\right]} \tag{20}$$

In computations, integrations along vertical lines at a fixed x [as, e.g., in (18)] are based both on the solution calculated at several internal points, for known boundary values at time t', and on interpolated values of the solution on the free surface and on the bottom, at the location x. Large variations of ν_o from time step to time step are prevented by using a moving average over 20 time steps of $\nu_o(t)$ values calculated with (20). Upper and lower bounds are also specified for ν_o to avoid both very large initial values, corresponding to small total energy in the beach, and small values, later, when the beach reaches a quasi-steady state and unwanted reflection could artificially decrease the incident energy flux (see details in the applications).

APPLICATIONS

Test and Validation of Periodic Wave Generation

A deepwater SFW of height $H_o' = 0.1$ and period $T' = 3.5515$ is first generated (i.e., cases 1, 2, and 4 in Table 1). Without an opposite current, this wave would have a mass transport $M_o' = M_oT/(\rho h_o^2) = 7.3610^{-3}$ (with $\overline{U_o'} = 2.022\ 10^{-3}$). After 11 iterations on the zero-mass-flux condition, (11) and (12), wave characteristics converge to $L' = 2.0324$, $T_L' = 3.6254$, $U' = -2.189\ 10^{-3}$ (Fig. 3), for a mass transport less than 10^{-13}. (This wave is significantly nonlinear, with a steepness H_o/L equal to about a third of the maximum steepness in deep water.) The computational domain is rectangular with length $l_D = 8h_o$ (case 1), $16h_o$ (case 2), or $24h_o$ [case 4; Fig. 4(a)]. Discretization parameters are given in Table 1. For case 4, for instance, the boundary is discretized with $N = 308$ nodes and $M = 272$ elements. There are $N_f = 241$ nodes on the free surface, with equal spacing $\Delta x_o' = 0.10 \simeq L'/20$, and 240 MCI elements; 32 quadratic elements are specified on the remaining part of the boundary. According to the Courant condition, $C_o = 0.4$, the initial time step is set to $\Delta t' = 0.04$. The tapering function $D(t)$ is specified over the first three periods of computations, that is, up to $t' = 10.65$. An AB of length $l' = 12 \simeq 6L'$ is used in these calculations (see next section for details concerning the AB).

Numerical errors for case 4 are plotted in Fig. 5(a), for the volume balance equation [(11)] ε_V, and the total energy balance in the tank ε_E (calculated using a similar equation). Both errors oscillate in time but, on average, $\varepsilon_V \simeq 0.002\%$ and $\varepsilon_E \simeq 0.006\%$, relative to the initial volume and potential energy of the computational domain, respectively. Such low average values confirm the accuracy of the generation of zero-mass-flux SFW in the model. [For the energy, larger errors occur during the first three periods of computations, for which the tapering function $D(t)$ is applied to the WB conditions, (9), thus (slightly) violating the FNPF governing equations.] Fig. 5(b) shows the trajectory of the first free-surface node/particle $[x_p(t), \eta_p(t)]$. As mentioned before, the WB follows the horizontal motion of this node and, due to differences between free-surface and depth-averaged horizontal velocities, the WB has a small net forward motion as a function of time. The initial transient front resulting from the tapering function is quite apparent in the figure, with both reduced wave elevation and particle motion [see also Fig. 4(b)]. For later times, the first node trajectory almost reaches a steady pattern. In the next section, we will see that reflection from the AB is very small [Fig. 4(c), curve a]. Hence, the small modulation of maximum surface elevation in Fig. 5(b) is due to differences in horizontal motion of the boundary over the Lagrangian and Eulerian periods, and not to reflection.

A wave with identical characteristics as in case 4 was generated using the flap WM, and a wave of height $H_o' = 0.15$ was also generated, both as a SFW (case 5) and using the WM. Figs. 6(a and b) show time series of normalized surface elevations η'/H_o' at $x' = 4$. For the SFWs, after the transient front has passed by, the wave shape reaches a nearly permanent form. WM-generated waves, however, exhibit temporal fluctuations. For $H_o' = 0.10$, these fluctuations are small but, for $H_o' = 0.15$, differences are larger, indicating the generation of higher-order harmonics. This is confirmed by results in Figs. 6(c and d): SFW harmonics do not fluctuate but, for WM-generated waves, the larger the wave height the larger the harmonics fluctuations. These results justify the need for the generation of SFWs in the model.

Test and Validation of Periodic Wave Absorption over Constant Depth

Adaptive energy absorption is validated by propagating SFWs of heights $H_o' = [0.1, 0.15, 0.20, 0.3]$ and length $L' \simeq [2, 6, 10]$, in tanks of constant depth h_o and lengths l_D, with

TABLE 1. Wave and Computational Data for 11 Cases of Zero-Mass-Flux SFWs Propagating over Constant Depth

Number (1)	H_o' (2)	T' (3)	T_L' (4)	L' (5)	U' ($\times 10^3$) (6)	l_D' (7)	l'/L' (8)	N (9)	M (10)	N_f (11)
1	0.10	3.5515	3.6254	2.0324	−2.189	8.0	1.97	116	98	81
2	0.10	3.5515	3.6254	2.0324	−2.189	16.0	1.97	212	184	161
3	0.15	3.5515	3.7177	2.0712	−4.791	16.0	1.93	212	184	161
4	0.10	3.5515	3.6254	2.0324	−2.189	24.0	5.91	308	272	241
5	0.15	3.5515	3.7177	2.0712	−4.791	24.0	5.80	308	272	241
6	0.10	10.622	10.630	10.033	−1.322	80.0	1.99	340	248	161
7	0.10	10.622	10.630	10.033	−1.322	80.0	3.99	340	248	161
8	0.30	10.622	10.708	10.261	−10.99	80.0	1.95	340	248	161
9	0.10	10.622	10.630	10.033	−1.322	120.0	5.98	500	368	241
10	0.30	10.622	10.708	10.261	−10.99	120.0	5.60	500	368	241
11	0.20	6.9490	7.0061	6.0388	−5.709	60.0	3.97	340	268	201

Note: Initial free-surface node spacing is $\Delta x_o' = l_D'/(N_f - 1) \simeq L'/20$, and initial time step is $\Delta t_o' = 0.4\Delta x_o'$; the upper bound for the AB coefficient is $\nu_o^{max} = 1.0$ and the lower bound is $\nu_o^{min} = 0.7 - 0.1l'/L'$.

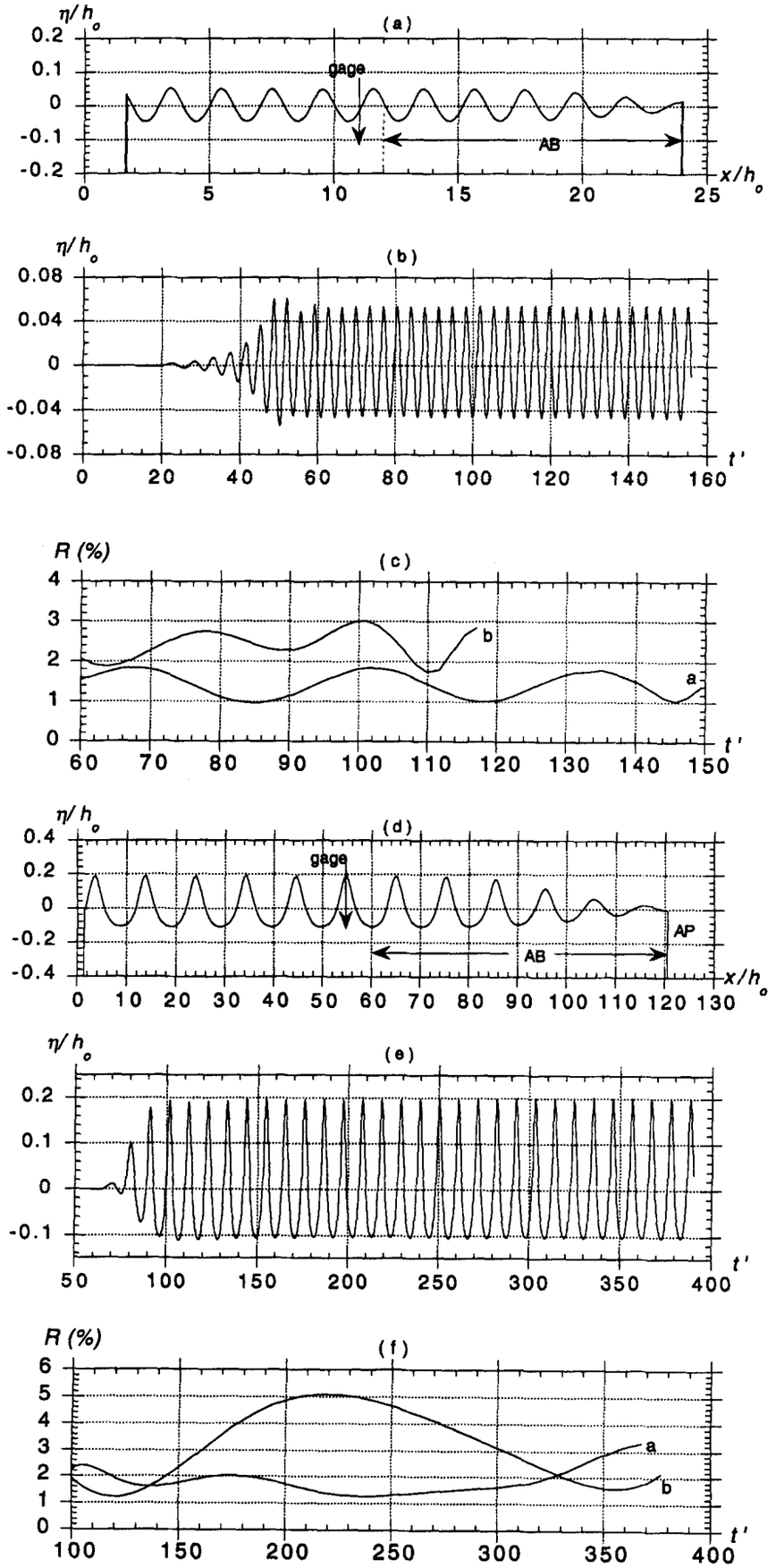

FIG. 4. Generation of Zero-Mass-Flux SFW with $H'_o = 0.1$ and $T' = 3.55$: (a)–(c) Case 4; (d)–(f) Case 10 (Table 1; $H'_o = 0.3$, $T' = 10.62$). [Computational Domain at t': (a) 155.98 or $43.9T'$; (d) 165.5 or $15.6T'$. Surface Elevation at x': (b) 11.0; (e) 55.0. Reflection Coefficient at x'_r: (c) 11.0, Case 4 (Curve a) and Case 5 (Table 1: $H'_o = 0.15$; Curve b); (f) 59.0, Case 10 (Curve b) and Case 9 (Table 1; $H'_o = 0.10$; Curve a)]

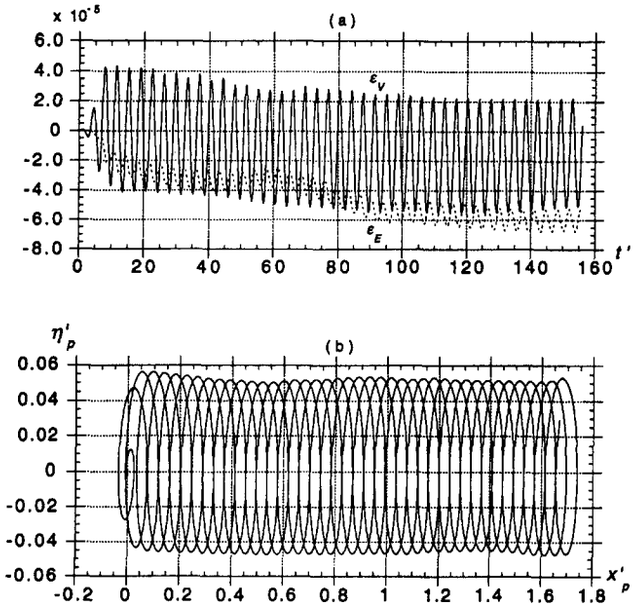

FIG. 5. Generation of Zero-Mass-Flux SFW with $H'_o = 0.1$ and $T' = 3.55$ (Case 4, Table 1): (a) Numerical Errors for Mass and Energy; (b) First Free-Surface Node Trajectory

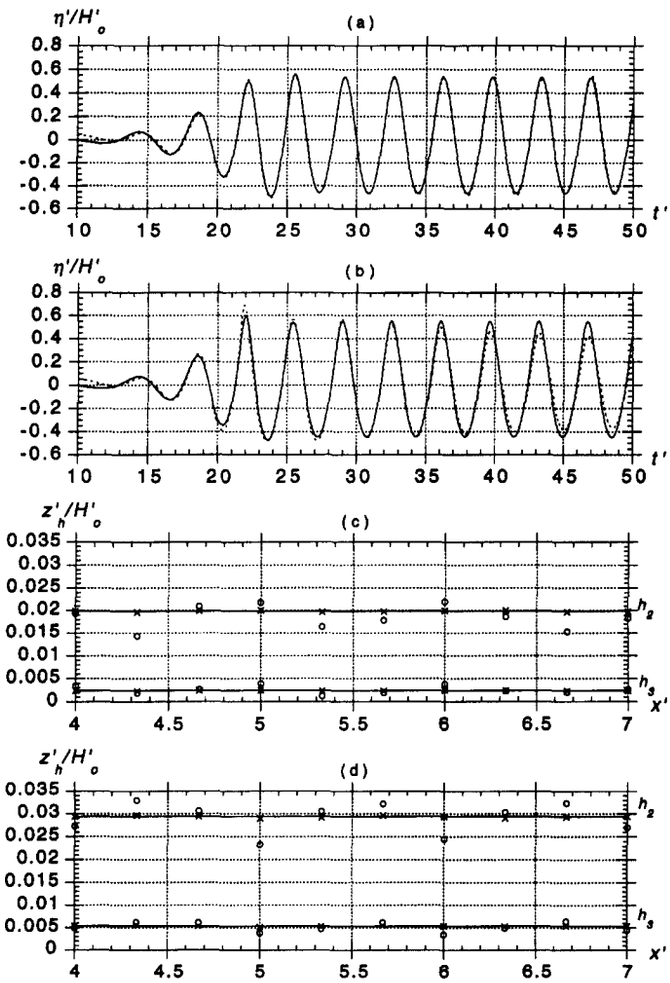

FIG. 6. Propagation over Constant Depth of Waves of Period $T' = 3.55$ and Height $H'_o = 0.10$ [(a), (c)]; and 0.15 [(b), (d)] [(——) (– × –) SFWs (Cases 4 and 5, Table 1); (- - - -) (○) Flap WM Generation. Surface Elevation at $x' = 4.0$: (a), (b); Amplitudes of Second (h_2) and Third (h_3) Harmonics Calculated over 20 Periods after Transient Front Has Passed By: (c), (d)]

an AB of length $l' \simeq [2, 4, 6]L'$ at their extremity (see Table 1 for parameter values and computational data). Energy absorption is achieved, either with an AB, or with an AB and an AP in combination. In each case, the (linear) reflection coefficient $R(t)$ is computed, using the three-gauge method by Mansard and Funke (1980), close to the AB entrance at $x'_r = x'_l - 1$, for $t' \geq t'^{\min}$, which represents the time for which computations reach a quasi-steady state. Computations are pursued up to time $t'^{\max}$ for which at least one reflection has occurred on each end of the numerical tank before the wave is recorded at x'_r. Table 2 gives average, minimum, and maximum reflection coefficients.

Detailed results are first analyzed for the short wave of case 4 [Figs. 4(a–c)], with an AB of length $l' = 12$ (i.e., about six times the incident-wave length) for $x' > x'_l = 12$ [Fig. (4a)], and no AP. An initial transient/dispersive front can be seen in Fig. 4(b), before wave height stabilizes at H'_o ($t' \simeq 65$), indicating low reflection from the AB. [Fig. 6(a) gives wave elevation at $x' = 4$ for the same wave and, as expected from wave theories, the dispersive front gradually spreads out between $x' = 4$ and 11.] Fig. 4(a) shows the free-surface profile after 43.9 periods of the wave propagation, that is, well after the transient front has been absorbed in the AB. A gradual amplitude decrease occurs within the AB but wave shape is very regular outside of the AB, indicating that a quasi-steady state has been reached for which reflection is small. This is confirmed in Fig. 4(c), where maximum reflection is less than 3% for both this case, and the larger wave of case 5 (see also Table 2). Other cases in Table 1 are discussed later in this section. (Similar computations, shown earlier in Fig. 6, indicated that the more irregular WM-generated waves were also well absorbed in the AB.)

Energy parameters for case 4 are given in Fig. 7. Fig. 7(a) shows both the instantaneous and period-averaged energy input in the AB over Δt, and the instantaneous energy absorbed in the AB. The denominator of (20), the AB adaptive energy balance, is denoted by E_{abs}/ν_o and both its instantaneous and period-averaged values are plotted. For $t' < 65$, the latter is smaller than the average energy input and, hence, $\nu_o = \nu_o^{\max} = 1$ and both E_{abs}/ν_o and E_{abs} are identical. For $t' > 65$, however, the energy balance (20) is activated and the beach coefficient adjusts its value within $0.1 < \nu_o(t) < 1$. Fig. 7(b) shows the total, potential, and kinetic energy in the domain and the cumulative absorbed energy in the AB. The first three of these reach fairly constant average values for $t' > 100$—indicating that a quasi-steady state has been reached—while the latter keeps increasing. In fact, for $t' > 97$, $\nu_o = \nu_o^{\min} = 0.1$ and the energy in the domain first stabilizes and then slowly decreases since there is slightly too much absorption in the AB [$E_{abs} > \overline{E_f \Delta t}$ in Fig. 7(a)]. This also results in a progressive reduction of $\overline{E_{abs}/\nu_o}$, the "absorbable" energy in the AB, and will eventually make ν_o stabilize to $\simeq \nu_o^{\min}$. (If no lower bound is set, ν_o keeps decreasing and waves build up in the AB, leading to increased reflection and to a further decrease in energy input; this rapidly makes the energy absorption procedure unstable.) Finally, for $t' > 110$, the total energy in the AB (with respect to its MWL) reaches an almost constant average value. These results validate the adaptive energy absorption procedure in the model.

Other cases in Tables 1 and 2 are discussed in the following. For cases 1–5, representing the shorter waves with $h_o/L \simeq 0.5$ (the linear deepwater limit), reflection from the AB is small (a few percent or less for both the average and maximum values), independent of wave height (case 5, in fact, is a very nonlinear wave with a steepness more than 50% the maximum), beach length, and duration of computations. As could be expected, no significant reduction in reflection occurs when using an AP in combination with the AB. Cases 6–11 repre-

TABLE 2. Reflection Coefficient at AB Entrance for 11 Cases Listed in Table 1

Number (1)	t'^{min}/T' (2)	t'^{max}/T' (3)	$\bar{R}$ (%) AB (4)	$\bar{R}$ (%) AB & AP (5)	R^{min} (%) AB (6)	R^{min} (%) AB & AP (7)	R^{max} (%) AB (8)	R^{max} (%) AB & AP (9)
1	6.14	13.0	1.32	1.22	0.85	0.62	2.52	2.41
2	14.5	25.9	1.64	1.63	0.29	0.30	2.57	2.50
3	13.4	21.4	2.44	2.24	0.88	0.85	4.87	3.66
4	15.8	43.9	1.32	1.30	0.82	0.82	1.82	1.85
5	15.9	34.1	2.42	2.25	1.60	1.40	3.02	2.62
6	9.55	26.4	18.8	2.81	1.71	1.15	38.5	3.98
7	9.52	26.4	6.86	2.05	1.70	0.38	19.0	3.65
8	9.55	26.4	21.7	3.95	1.75	0.85	40.0	5.80
9	12.3	35.8	4.57	1.86	1.31	1.21	9.52	3.15
10	12.0	38.1	4.89	3.24	1.46	1.25	9.91	5.15
11	10.7	33.1	5.42	1.85	1.54	0.25	10.3	2.85

Note: $\bar{R}$, R^{min}, and R^{max} denote average, minimum, and maximum values, respectively [computed with the method by Mansard and Funke (1980) for gauges located at $(x_l' - 1.2, x_l' = x_l' - 1, x_l' - 0.7)$], after computations have reached a quasi-steady state, i.e., for time, $t'^{min} < t' < t'^{max}$; AB and AB & AP denote absorbing beach alone and AB with the absorbing piston specified at the beach extremity, respectively.

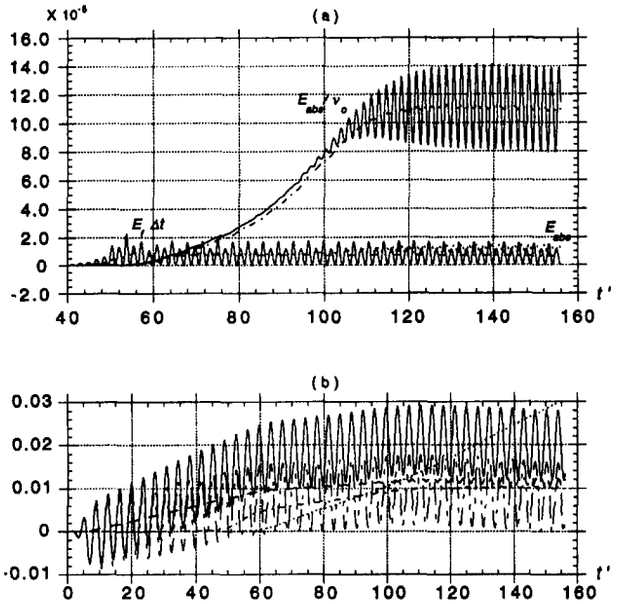

FIG. 7. Same Case as in Fig. 5: (a) (——) Energy Input $E_I\Delta t$ and Absorption (- - - -) $E_{abe} = E_{In}\Delta t$, in AB [(—·—·) Denote Period-Averaged Quantities, $\overline{E_I\Delta t}$ and $\overline{E_{abe}/\nu_o}$]; (b) Energy Components in Computational Domain: (——) Total Energy E; (— —) Kinetic Energy E_K; (— · —) Potential Energy E_P; (- - - -) Cumulative Energy Absorbed in AB, E_{abeT}; and (—·—·) Total Energy in AB with Respect to AB's MWL, E_{TABo}

sent longer (intermediate depth) waves, with $h_o/L \simeq 0.097 - 0.17$. In cases 6 and 8, reflection becomes very large when using an AB of length only twice the wavelength (and no AP), increasing from a few percent at $t' = 130$ (first reflection) to about 40% for $t' > 230$ (second reflection). In case 7, maximum reflection is reduced by a factor of two and average reflection is down to 7% (despite ν_o^{min} being also reduced), when using an AB of length four times the wavelength (and no AP), for the same wave as in case 6. In cases 9 and 10, further reductions of the maximum reflection (by a factor of two to less than 10%) and of the average reflection (to less than 5%) are achieved when using an AB of length six times the wavelength. In case 11, finally, reflection varies between 1.5 and 10% for average values of both the wave and AB parameters.

For the longer waves (cases 6–11), low reflection can be achieved with a short AB, only when using an AP at the extremity; in this case, both the average and maximum reflection become a few percent or less (Table 2). Detailed results are given in Figs. 4(d–f) for such a case (case 10, a fairly nonlinear wave), with an AB of length six times the wavelength and an AP. Fig. 4(e) shows wave elevation at $x' = 55$; for this fairly long wave, dispersion is quite small after the first three tapered waves have passed by. The wave profile thus quickly reaches a quasi-steady state, indicative of small reflection. Fig. 4(d) shows the free-surface profile after 15.6 periods, when computations are quasi-steady; waves clearly gradually decrease in the AB. Fig. 4(f), finally, shows the reflection coefficients for both $H_o' = 0.1$ (case 9) and 0.30 (this case). Maximum reflection is less than 5% for both waves.

For all cases, high absorption is thus achieved in the tank when using an AB of length about three to four times the incident-wave length, in combination with an AP at the tank extremity. This setup is used in the following shoaling computations.

Periodic Wave Shoaling over Plane Slope

Shoaling of a zero-mass-flux SFW of height $H_o' = 0.06$ and period $T' = 5.5$ ($U' = -0.00576$ and $L_o' = 4.321$) is calculated over a 1:50 slope, in the domain sketched in Fig. 1, with an AB of initial length $l' = 10$, for $x_l' \geq 50$, and an AP at the tank extremity. The water depth at x_l' is $0.10h_o$ and is gradually increased in the AB to $h_1 = 0.5h_o$, following a "tanh-like" bottom variation. Due to shoaling, wavelength reduces to $L' = 2.12$ at $x' = 50$ [Fig. 8(a)]; accordingly, the AB length is about four times the wavelength. (Note, $h/L < 0.05$ at the AB entrance, which is in the shallow water region for the incident wave.) The initial computational domain is discretized with $N = 578$ nodes and $M = 476$ boundary elements. There are $N_f = 385$ nodes on the free surface, with equal initial spacing $\Delta x_o' = 0.155$ (i.e., 36 nodes per incident-wave length), defining 384 MCI elements; 92 quadratic elements are used on the remaining part of the boundary. With these data, the CPU time is 67 s per time step on a Sparc ULTRA 1 workstation (SPECft $\simeq$ 350). The initial time step is $\Delta t' = 0.06$, and 4,500 (varying) time steps are calculated for this case.

As waves become steep toward the top of the slope, discretization nodes may get quite close to each other and create almost singular values for the BEM integrals, leading to poor accuracy. In such situations, the adaptive regridding method by Grilli and Subramanya (1996) is used to automatically regrid nodes three by three when the distance between two nodes is either more than four times or less than 0.25 times the distance between the previous two nodes.

Ten "numerical" gauges are specified over the slope to calculate shoaling wave characteristics. Figs. 8(b–e) show wave elevations calculated at the last four gauges, referred to as g1

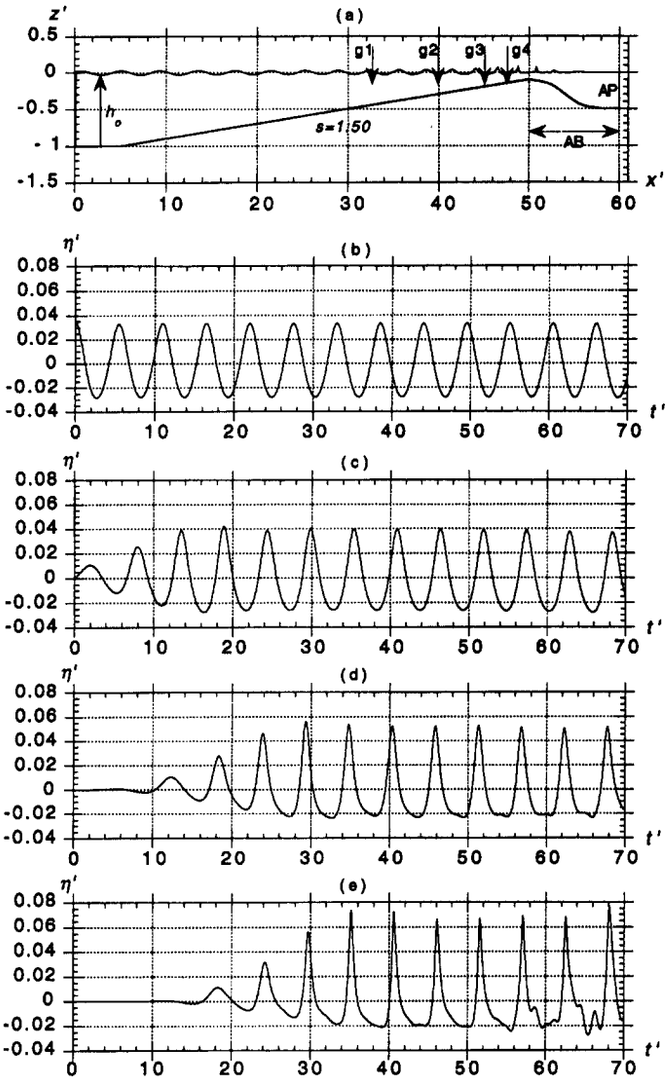

FIG. 8. Shoaling of Zero-Mass-Flux SFW over 1:50 Slope, with $H'_o = 0.06$ and $T' = 5.5$: (a) Free-Surface Elevation at $t' = 79.6$ and Marked Locations of Four Gauges, g1–g4 at $x' = 32.5$, 40, 45, and 47.5, Respectively; (b)–(e) Surface Elevations at Gauges g1–g4, Respectively (Time Set to Zero When Largest Wave Crest in Initial Front Crosses g1)

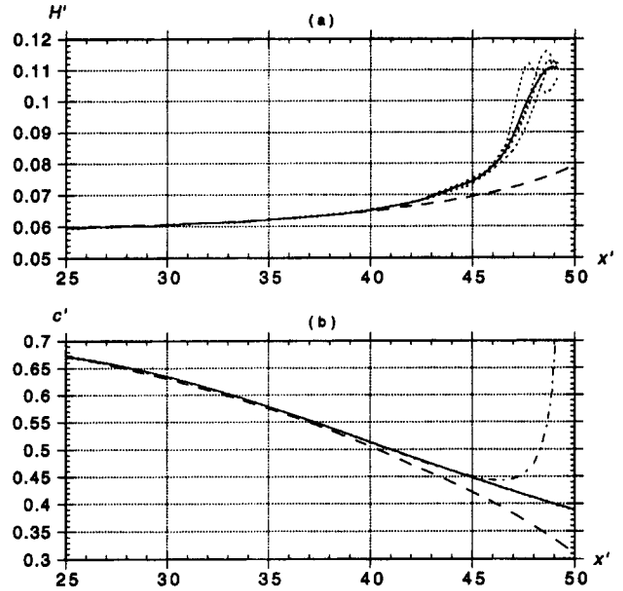

FIG. 9. Same Computations as in Fig. 8: (a) Wave Height; (b) Cererity over Slope for (- - - -) Seventh to 10th Incident Waves; (——) Average of Seventh to 10th Incident Waves; (– – –) Linear Theory; (– – –) Third-Order Stokes Theory

to g4 in Fig. 8(a). Wave height and asymmetry gradually increase toward the top of the slope, as water shallowness more significantly affects wave shape. The spreading out of the dispersive front is also clear on the figures; after the front has passed by the gauges, results reach a fairly steady pattern, indicating small reflection [except for some small high-frequency oscillations in Fig. 8(e)].

Wave height $H'(x')$ and (crest) celerity $c'(x') = c/\sqrt{gh_o}$ were calculated for successive incident waves shoaling over the slope (see seventh to 10th waves in Fig. 9). The good agreement of results for successive waves indicates that absorption in the AB/AP is effective and that the model has reached a quasi-steady state, for which shoaling wave properties can be calculated. Significant differences can be seen in Fig. 9 between FNPF results and linear theory, for $x' > 40$, which corresponds to $h/L < 0.106$ ($H/h > 0.22$, $H/L > 0.023$). For smaller depth, due to increased nonlinearity, both wave height and celerity become larger than predicted by linear wave theory (by up to 31% and 19%, respectively, at $x' = x'_l$). Third-order Stokes theory quite well predicts celerity up to $x' = 45$ ($H/h = 0.37$, $h/L = 0.081$), but diverges for shallower water.

At the AB entrance, $x' = x'_l$ ($h/L = 0.047$), wave-averaged FNPF results (Fig. 9) give $H/h = 0.93$ and $H/L = 0.052$ (linear theory would give $H/h = 0.64$ and $H/L = 0.045$). Linear wave theory combined to an empirical breaking criterion (Dean and Dalrymple 1984) would predict breaking wave characteristics as $H_b/h_b = 0.90$ and $H/L = 0.048$. Hence, FNPF results correspond to a slightly steeper wave, which should thus be quite close to breaking. Computations for a larger incident wave with $H'_o = 0.08$, indeed, would show that the largest wave in the transient front overturns and breaks at the AB entrance.

Other similar shoaling computations over gentle slopes were performed by Grilli and Horrillo (1997), and both local and integral wave properties were calculated and analyzed. Differences with linear and weakly nonlinear wave theories were discussed. The reader is invited to consult this paper for further details.

CONCLUSIONS

New methods for generating and absorbing zero-mass-flux SFWs were implemented and validated in a FNPF NWT. The NWT was then used to calculate wave shoaling over a gentle slope.

It was found that waves could propagate without change of form in the NWT, while closely achieving constant water volume. Waves of similar characteristics generated by a flap wavemaker exhibited both spatial and temporal modulations, indicative of higher harmonics generation.

For short waves propagating over constant depth, energy absorption in the AB was high (greater than 97%), even with a beach length only two times the wavelength; absorption was good for both SFWs and flap-generated, that is, slightly irregular, waves. For longer waves, high absorption values were only achieved when using an AB, with a length two to four times the wavelength, in combination with an AP at the tank extremity. (Even higher absorption values could be achieved using longer ABs but the computational cost would be increased.) Such results are due to the nature of energy absorption in the AB (i.e., the counteracting pressure), which essentially affects wave kinematics close to the free surface and thus better absorbs the energy of short waves for which horizontal velocity is larger close to the free surface. For longer waves,

horizontal velocity is more uniform over depth, and energy is better absorbed by the AP condition.

For shoaling waves, absorption was also good when using an AB/AP and gradually increasing the depth in the AB (hence causing deshoaling). Thus, shoaling of periodic waves was modeled over a gentle slope, up to very close to the breaking point, and a quasi-steady state was reached in the NWT for which fully nonlinear wave properties were obtained (i.e., wave profiles, height, and celerity variations).

Finally, since adaptive absorption in the AB/AP, defined by (13)–(20), does not require period T to be constant, irregular incident waves could likely be absorbed in this NWT. For each incident wave, the period would have to be calculated, for example, using a zero up-crossing method. Such irregular waves could be generated, for instance, using the second-order method proposed by Schäffer (1996). This, however, is beyond the scope of the present paper and is left for further studies.

ACKNOWLEDGMENTS

This research was supported by NRL-SSC, under grant N00014-94-1-G607 from the U.S. Department of the Navy, Office of the Chief of Naval Research. The information reported in this work does not necessarily reflect the position of the U.S. Government.

APPENDIX. REFERENCES

Brebbia, C. A. (1978). *The boundary element method for engineers*. John Wiley & Sons, London, U.K.

Brorsen, M., and Larsen, J. (1987). "Source generation of nonlinear gravity waves with the boundary integral method." *Coast. Engrg.*, 11, 93–113.

Cao, Y., Beck, R. F., and Schultz, W. W. (1993). "An absorbing beach for numerical simulations of nonlinear waves in a wave tank." *Proc., Eighth Int. Workshop Water Waves and Floating Bodies*, 17–20.

Chapalain, G., Cointe, R., and Temperville, A. (1996). "Observed and modeled resonantly interacting progressive water-waves." *Coast. Engrg.*, 16, 267–300.

Clément, A. (1996). "Coupling of two absorbing boundary conditions for 2D time-domain simulations of free surface gravity waves." *J. Comp. Phys.*, 126, 139–151.

Cointe, R. (1990). "Numerical simulation of a wave channel." *Engrg. Anal. with Boundary Elements*, 7(4), 167–177.

Cooker, M. J. (1990). "A boundary-integral method for water wave motion over irregular bed." *Engrg. Anal. with Boundary Elements*, 7(4), 205–213.

Dalrymple, R. A. (1976). "Wave-induced mass transport in water waves." *J. Wtrwy., Port, Coast., and Oc. Engrg.*, ASCE, 102(2), 255–264.

Dean, R. G., and Dalrymple, R. A. (1984). *Water wave mechanics for engineers and scientists*. Prentice-Hall, Englewood Cliffs, N.J.

Dold, J. W., and Peregrine, D. H. (1986). "An efficient boundary integral method for steep unsteady water waves." *Numerical methods for fluid dynamics II*, K. W. Morton and M. J. Baines, eds., Clarendon Press, Oxford, U.K., 671–679.

Dommermuth, D. G., Yue, D. K. P., Lin, W. M., Rapp, R. J., Chan, E. S., and Melville, W. K. (1988). "Deep-water plunging breakers: A comparison between potential theory and experiments." *J. Fluid Mech.*, 189, 423–442.

Engquist, B., and Majda, A. (1977). "Absorbing boundary conditions for the numerical simulation of waves." *Math. Comp.*, 31, 629–651.

Grilli, S. T., and Horrillo, J. (1997). "Nonlinear properties of waves shoaling over slopes and natural beaches." *Proc., 25th Int. Conf. on Coast. Engrg.*, Vol. 1, ASCE, New York, N.Y., 717–730.

Grilli, S. T., Skourup, J., and Svendsen, I. A. (1989). "An efficient boundary element method for nonlinear water waves." *Engrg. Anal. with Boundary Elements*, 6(2), 97–107.

Grilli, S. T., and Subramanya, R. (1994). "Quasi-singular integrations in the modelling of nonlinear water waves." *Engrg. Anal. with Boundary Elements*, 13(2), 181–191.

Grilli, S. T., and Subramanya, R. (1996). "Numerical modeling of wave breaking induced by fixed or moving boundaries." *Comp. Mech.*, 17, 374–391.

Grilli, S. T., Subramanya, R., Svendsen, I. A., and Veeramony, J. (1994). "Shoaling of solitary waves on plane beaches." *J. Wtrwy., Port, Coast., and Oc. Engrg.*, ASCE, 120(6), 609–628.

Grilli, S. T., and Svendsen, I. A. (1990). "Corner problems and global accuracy in the boundary element solution of nonlinear wave flows." *Engrg. Anal. with Boundary Elements*, 7(4), 178–195.

Grilli, S. T., Svendsen, I. A., and Subramanya, R. (1997). "Breaking criterion and characteristics for solitary waves on plane beaches." *J. Wtrwy., Port, Coast., and Oc. Engrg.*, ASCE, 123(2), 102–112.

Israeli, M., and Orszag, S. A. (1981). "Approximation of radiation boundary conditions." *J. Comp. Phys.*, 41, 115–135.

Klopman, G. (1988). "Numerical simulation of gravity wave motion on steep slopes." *Delft Hydr. Rep. No. H195*, Delft, The Netherlands.

Larsen, J., and Dancy, H. (1983). "Open boundaries in short waves simulations—A new approach." *Coast. Engrg.*, 7, 285–297.

Le Mehauté, B. (1972). "Progressive wave absorber." *J. Hydr. Res.*, 10(2), 153–169.

Lin, W. M., Newman, J. N., and Yue, D. K. (1984). "Nonlinear forced motion of floating bodies." *Proc., 15th Int. Symp. on Naval Hydrodynamics*, Hamburg, Germany.

Longuett-Higgins, M. S., and Cokelet, E. D. (1976). "The deformation of steep surface waves on water—I. A numerical method of computation." *Proc., Royal Soc. London*, London, U.K., A350, 1–26.

Mansard, E. P., and Funke, E. R. (1980). "The measurement of incident and reflected spectra using a least square method." *Proc., 17th Int. Conf. on Coast. Engrg.*, Vol. 1, ASCE, New York, N.Y., 154–172.

Mei, C. C. (1989). *The applied dynamics of ocean surface waves*, Second Ed., World Scientific, River Edge, N.J.

New, A. L., McIver, P., and Peregrine, D. H. (1985). "Computation of overturning waves." *J. Fluid Mech.*, 150, 233–251.

Ohyama, T., and Nadaoka, K. (1991). "Development of a numerical wave tank for analysis of nonlinear and irregular wave fields." *Fluid Dynamic Res.*, 8, 231–251.

Ohyama, T., and Nadaoka, K. (1994). "Transformation of a nonlinear wave train passing over a submerged shelf without breaking." *Coast. Engrg.*, 24, 1–22.

Orlanski, I. (1976). "A simple boundary condition for unbounded hyperbolic flows." *J. Comp. Phys.*, 21, 251–269.

Otta, A. K., Svendsen, I. A., and Grilli, S. T. (1992). "Unsteady free surface waves in region of arbitrary shape." *CACR, Res. Rep. 92-10*, Univ. of Delaware, Newark, Del.

Romate, J. (1992). "Absorbing boundary conditions for free surface waves." *J. Comp. Phys.*, 99, 135–145.

Schäffer, H. A. (1996). "Second-order wavemaker theory for irregular waves." *Oc. Engrg.*, 23, 47–88.

Sommerfeld, A. (1949). *Partial differential equations in physics*. Academic Press, New York, N.Y.

Subramanya, R., and Grilli, S. T. (1994). "Kinematics and properties of fully nonlinear waves shoaling and breaking over a gentle slope." *Proc., Int. Symp. on Waves—Phys. and Numer. Modeling*, M. Isaacson and M. Quick, eds., IAHR, 1106–1115.

Svendsen, I. A., and Grilli, S. T. (1990). "Nonlinear waves on steep slopes." *J. Coast. Res.*, 7, 185–202.

Vinje, T., and Brevig, P. (1981). "Numerical simulation of breaking waves." *Adv. Water Res.*, 4, 77–82.